



HAL
open science

Mapping of the Electrostatic Potentials in a Fully Processed Led Device with nm-Scale Resolution by In Situ off-Axis Electron Holography

David Cooper, Christophe Licitra, Younes Boussadi, Badhise Ben-bakir,
Bruno Masenelli

► **To cite this version:**

David Cooper, Christophe Licitra, Younes Boussadi, Badhise Ben-bakir, Bruno Masenelli. Mapping of the Electrostatic Potentials in a Fully Processed Led Device with nm-Scale Resolution by In Situ off-Axis Electron Holography. *Small Methods*, 2023, 7 (9), 10.1002/smt.202300537. hal-04121019

HAL Id: hal-04121019

<https://hal.science/hal-04121019>

Submitted on 7 Jun 2023

HAL is a multi-disciplinary open access archive for the deposit and dissemination of scientific research documents, whether they are published or not. The documents may come from teaching and research institutions in France or abroad, or from public or private research centers.

L'archive ouverte pluridisciplinaire **HAL**, est destinée au dépôt et à la diffusion de documents scientifiques de niveau recherche, publiés ou non, émanant des établissements d'enseignement et de recherche français ou étrangers, des laboratoires publics ou privés.

Mapping of the Electrostatic Potentials in a Fully Processed Led Device with nm-Scale Resolution by In Situ off-Axis Electron Holography

David Cooper,* Christophe Licitra, Younes Boussadi, Badhise Ben-Bakir, and Bruno Masenelli

The optoelectronic properties of a fully processed red emitting AlGaInP micro-diode device is measured using standard I-V and luminescence measurements. A thin specimen is then prepared for in situ transmission electron microscopy analysis by focused ion beam milling, then the changes of electrostatic potential as a function of applied forward bias voltage are mapped by off-axis electron holography. We demonstrate that the quantum wells in the diode sit on a potential gradient until the threshold forward bias voltage for light emission is reached; at which point the quantum wells are aligned at the same potential. From simulations, a similar effect for the band structure can be demonstrated, where the quantum wells are aligned at the same energy level, and contain electrons and holes that are available for radiative recombination at this threshold voltage. We demonstrate that off-axis electron holography can be used to directly measure the potential distribution in optoelectronic devices, and is a powerful tool to help better understand their performance and to improve simulations.

Whereas LED efficiency has been continuously improved over the years, their miniaturization at the micrometer size is challenging as the pixels are more susceptible to edge effects which degrade their quantum efficiency and increase leakage current.^[5,6] It is thus essential to be able to identify and map not only edge defects but those that appear in the bulk of the devices in order to estimate and distinguish the impact of each type and remove them. Of prime importance are the structural defects such as threading dislocations or antiphase boundaries.^[7,8] These are extended defects that usually result from a lattice mismatch or surface roughness of the substrate. They can extend through the active region, through multiple quantum wells (QW) and quench the radiative


1. Introduction

Light emitting diodes (LEDs) are widespread in daily life, from indoor and outdoor domestic lighting, flat panel displays and data communication. They are currently being developed for virtual reality applications (micro-LEDs),^[1,2] or for sanitization.^[3,4]

recombination. Such defects can be observed relatively easily using transmission electron microscopy (TEM). However, point defects such as vacancies or interstitials are more difficult to image. These defects often behave as charge traps and may modify the electrostatic potential within devices as such it would be desirable to measure their impact on the operation of a device. Off-axis electron holography is a TEM based technique that measures the phase of the electrons that have passed through a region of interest. As the phase of an electron is sensitive to the electrostatic potential, then this is a unique method of locally measuring the potential at the required spatial resolution.

D. Cooper, C. Licitra, Y. Boussadi, B. Ben-Bakir
Univ. Grenoble Alpes
38000 Grenoble, France
E-mail: david.cooper@cea.fr

B. Masenelli
Univ. Lyon
INSA Lyon
CNRS
Ecole Centrale de Lyon
Université Claude Bernard Lyon 1
INL, UMR5270, 69621 Villeurbanne, France

 The ORCID identification number(s) for the author(s) of this article can be found under <https://doi.org/10.1002/smt.202300537>

© 2023 The Authors. Small Methods published by Wiley-VCH GmbH. This is an open access article under the terms of the Creative Commons Attribution-NonCommercial-NoDerivs License, which permits use and distribution in any medium, provided the original work is properly cited, the use is non-commercial and no modifications or adaptations are made.

DOI: 10.1002/smt.202300537

Much effort has been devoted to study the composition and geometry-related defects in LEDs using standard TEM.^[9–12] Pioneering studies to measure the potentials in IIIV materials by electron holography were performed > 20 years ago with poor stability of the TEMs, less powerful computing resources and most importantly before the widespread use of dual-beam focused ion beam (FIB) milling tools for specimen preparation.^[13,14] For GaN QW structures, a combination of different advanced analysis modes provided by TEM and performed in parallel with electron holography has proven valuable to map the polarization fields and strain in relation with composition inhomogeneity.^[15–19] Today it is possible to revisit these experiments with more powerful microscopes, better processing tools and routine FIB preparation.^[20–22] However, more importantly, all previous examples in the literature are observations of static LED devices. To be

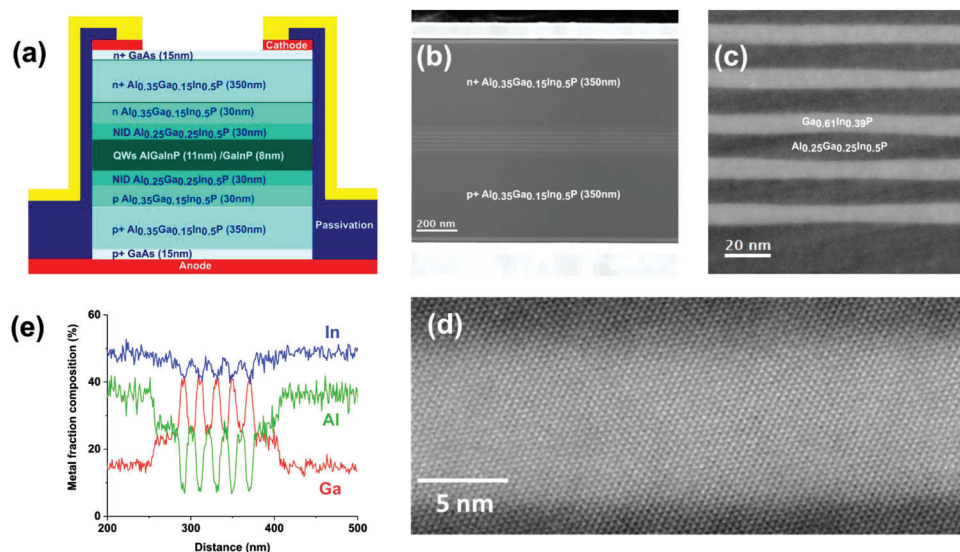


Figure 1. a) The intended structure of the AlGaInP diode. b–d) HAADF images and e) EDX profiles across the region of interest. (The HAADF STEM and EDX were performed on a separate region of the specimen after the holography experiments to avoid damaging the specimen).

able to understand better how these devices work and improve them, it would be advantageous to be able to directly measure the electrostatic potential dynamically during electrical biasing with nm-scale resolution. This would allow one to see how the internal potentials in the device are affected by the presence of defects during operation and infer how the charge flow is affected.

In these experiments, a fully processed 56 μm -sized Al-GaInP micro-LED device has been characterized ex situ using current–voltage–luminance (IVL) measurements and photoluminescence (PL) to observe the diode behavior and light emission. A TEM specimen was then prepared from the micro-LED and the electrostatic potential was observed dynamically during operation by off-axis electron holography. The measurements of the potential were then compared to simulations to better understand how the potential affects the radiative recombination in the device. The micro-LED chosen for these studies was a device with known good opto-electronic properties such that the results by electron holography could be more easily interpreted.

1.1. Standard Device Characterization

One of the advantages of using TEM to perform characterization is its versatility. It is possible to make atomic resolution structural mapping by aberration corrected high angle annular dark field (HAADF) imaging and compositional mapping by energy dispersive X-ray spectroscopy (EDX) to verify that the device was as expected. **Figure 1a** shows a schematic of the micro-LED device examined.^[23] **Figure 1b–d** shows HAADF images at increasing magnification demonstrating that the GaInP quantum wells have the correct dimension, but also have a wavy structure. **Figure 1d** demonstrates the growth quality and crystalline properties of the QWs. **Figure 1e** shows an EDX measurement of the metal fraction composition, revealing that Al is present in the QWs which was unintended.

The electro-optical properties of the device are shown in **Figure 2**. A sequence of images of the diode at 2.0, 3.0, and 4.0 V can be seen in **Figures 2a–c**, respectively. The position of the region of the diode that was examined by TEM is indicated in **Figure 2a**. It can be seen that at 2.0 V the emission is even across the device, even though it is relatively low. Once 3.0 V is reached, the regions that are closer to the cathode regions reach saturation, while the regions in the center of the diode exhibit lower emission. This is directly related to the inhomogeneous spreading of the electric field in the device.^[24] The electric field, and therefore, the charge carrier injection are higher close to the electrodes. At a forward bias of 4.0 V, the whole device is emitting near saturation. **Figure 2d** shows the ex situ measurements of the IV characteristics and luminance of the device. Here it can be seen that the diode begins to draw current at a forward bias voltage of 1.0 V, but light emission does not occur until a threshold voltage of > 1.5 V. Finally, **Figure 2e** shows the measured emission spectra of the diode compared to simulations from the expected structure indicating a red shift of 15 nm due to both the influence of the mis-orientation of the GaAs substrate and waviness of the QWs in the micro-LEDs.

1.2. Specimen Preparation

Figure 3a–f shows scanning electron microscopy (SEM) images of the specimen as it was prepared by FIB milling. A chip containing many devices was loaded into the FIB and a device with known good properties was selected for preparation. An electron transparent lamella was extracted from along the center of the device using in situ lift out. To reduce damage of the surfaces, the FIB was operated at 16 kV. The specimen was then welded using W deposition to a dedicated chip for in situ biasing in the TEM by ion beam assisted deposition (IBAD). A parallel-faced 355 nm thick specimen was then prepared for observation by electron holography. Isolation cuts were made in the indicated

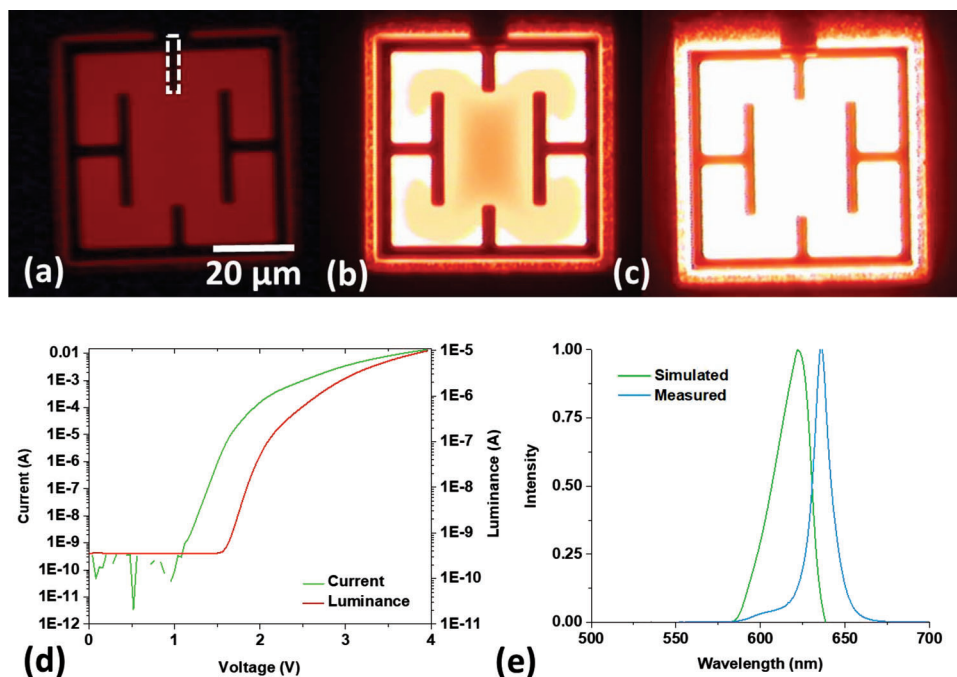


Figure 2. a–c) Images of the diode at forward bias voltages of 2.0, 3.0, and 4.0 V, respectively. d) Measurements of the IV and luminance of the diode performed ex situ. e) Simulated and measured emission spectra from the device.

regions such that the voltage could be applied to the top and bottom electrodes without short circuits occurring. The choice of using a very thick sample was made to reduce effects arising from surface damage and charging which can dominate the measurement of the potentials in thin specimens.^[25] A second region indicated in Figure 3f was further thinned to 150 nm for HAADF STEM and EDX observation. The regions of interest were then cleaned using 2 kV Ga ions to reduce the conducting Ga-implanted surfaces. Figure 3g shows a HAADF STEM image of the region of sample that was observed by electron holography. After all the TEM experiments, we successfully verified that the micro-LED was still emitting light.

1.3. Off-Axis Electron Holography

A schematic of off-axis electron holography is shown in Figure 4a.^[26] A coherent electron wave that passed through the specimen is interfered by a positively charged electron biprism with a reference wave that has passed through vacuum. From the position of the fringes, the phase of the electrons can be recovered by using a simple Fourier reconstruction technique. If the specimen is tilted from a zone axis to reduce the dynamical diffraction effects, then the change in phase is directly proportional to both the Mean Inner Potential of the material (V_{MIP}) and variations of the electrostatic potential arising from the presence of active dopants (V_{dopant}). The measured change in phase is given by,

$$\Delta\Phi = C_E \int_0^t (V_{\text{dopant}} + V_{\text{MIP}}) dz \quad (1)$$

where t is the thickness of the specimen and C_E is a constant equal to $0.0073 \text{ rad}\cdot\text{nm}^{-1}\cdot\text{V}^{-1}$ for 200 kV electrons.^[27] The MIP is the volume averaged electrostatic potential of a material.^[28] This is an intrinsic property which depends on the composition, structure, strain and bonding. The values of V_{MIP} can be obtained either by the independent atom model,^[29] or by density functional theory (DFT) calculations that account for bonding.^[30] The exact values of the V_{MIP} are difficult to obtain experimentally due to problems in measurement of the absolute phase change of the electrons in real materials that are not weak phase objects.^[31] Experimental measurements do exist and are 14.4 and 14.5 V for GaP and InP, respectively.^[32] In addition, DFT calculations have been used to obtain values of 11.39 for AlP, 13.6 for GaP and 13.9 for InP.^[33] These values suggest that a higher MIP is expected to be measured in the InGaP QW structures compared to the AlGaInP interlayers that will allow the “brighter” QWs to be easily identified during the electron holography experiments. An additional consequence of the MIP is that its magnitude is typically an order of magnitude higher than the expected signal from active dopants. As such, a high quality parallel-sided and flat lamella specimen is required to avoid changes in the MIP dominating the measurements.

It is important to consider the effect of specimen preparation on the experiments. It is well known that the use of high energy Ga ions during FIB preparation will modify the specimen surfaces by forming both Ga implanted conducting amorphous layers,^[34–39] and near surface layers that have high concentrations of defects that can lead to inactive dopant atoms.^[40] The charging of these defected layers lead to the presence of depletion regions at the surfaces of the samples.^[41] This are known as the inactive thickness that leads to a measured step in potential that is less than expected from theory. The presence of these inactive layers

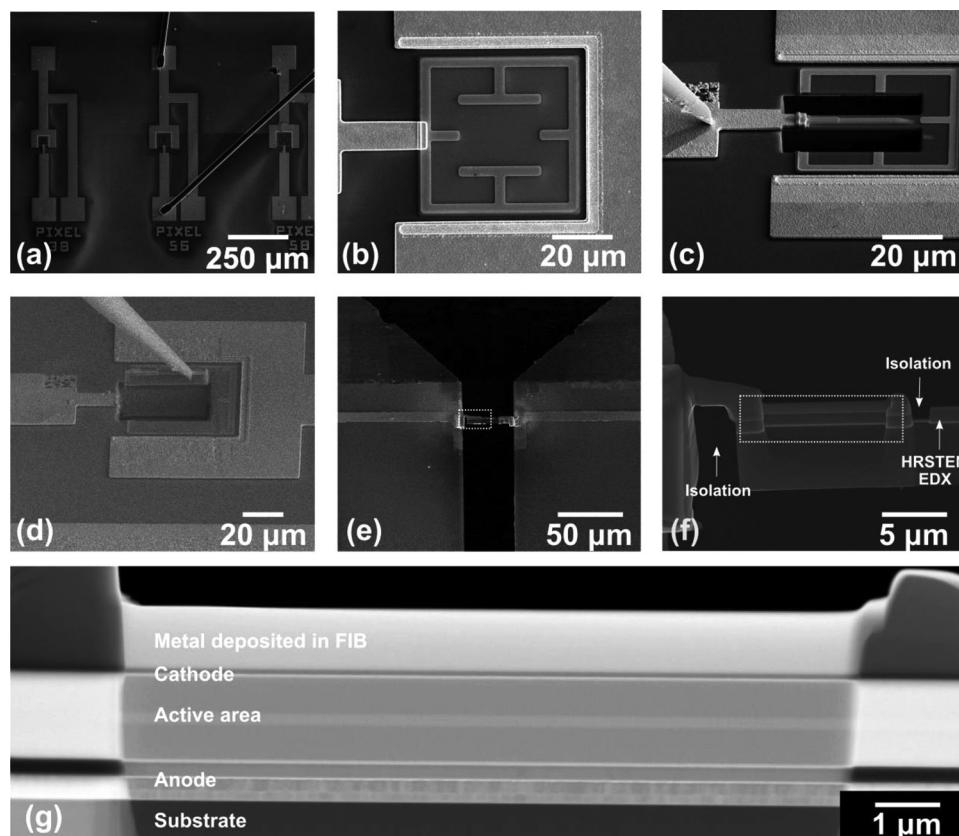


Figure 3. SEM images of the key steps during specimen preparation in the FIB. a) The chip containing many devices is loaded into the FIB and b) the device of interest is located. c) The region under the top metal cathode is isolated and d) removed for TEM observation. e) The lamella is welded to a dedicating chip for in situ biasing using metal deposition. f) Shows the region indicated by the dashed rectangle in (e), FIB cuts are made to isolate the top and bottom contacts such there is no short circuit across the region of interest. Here a thick region was electrically isolated for the electron holography experiments and a thinner area indicated was also milled for measurements of the structure and chemistry by HAADF STEM and EDX. g) Shows the region indicated by the dashed rectangle in (f). In this case a HAADF image of the finished sample and the entire region that was available for measurement is shown. The electron holograms were acquired from the center of this region.

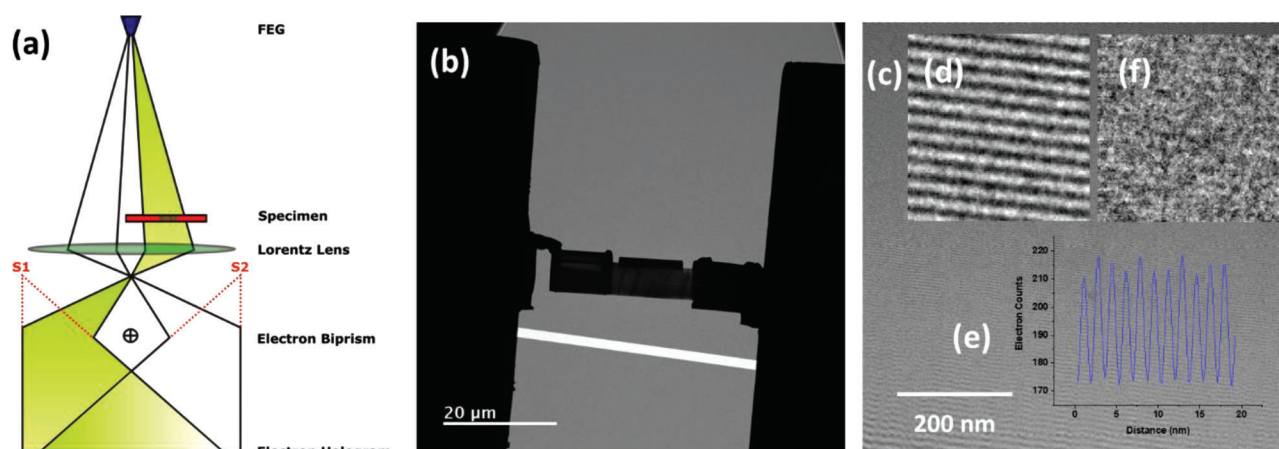


Figure 4. a) Schematic of electron holography. b) Low magnification image of the specimen attached to the biasing chip. The electron hologram can be seen by the bright stripe. c) A reference electron hologram d) and detail with a field of view of 770 nm and fringe spacing of 1.6 nm. e) Profiles taken across the reference hologram. f) Detail of object electron hologram through the 355 nm thick specimen.

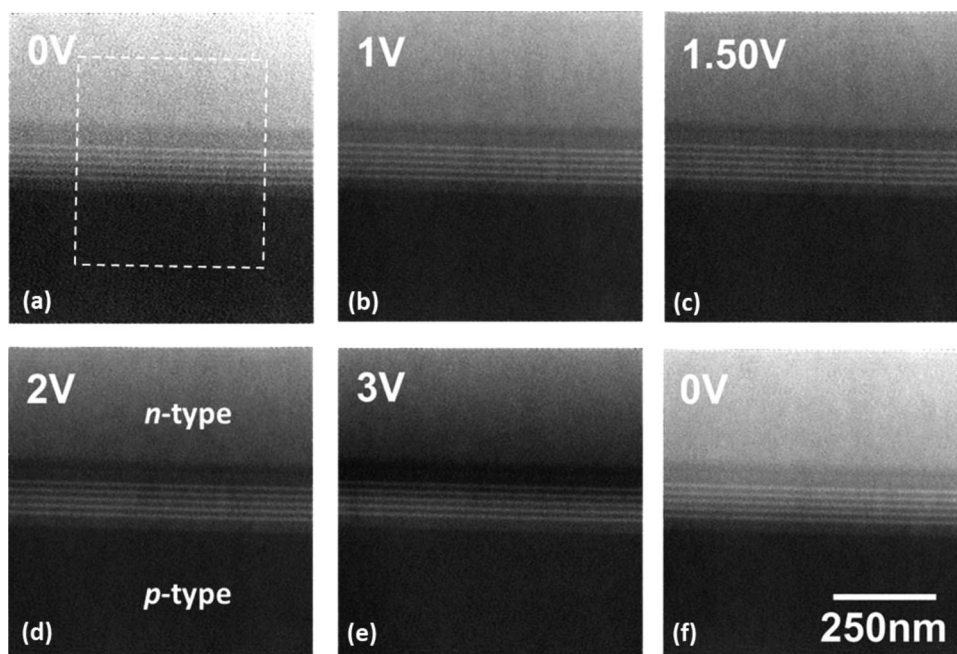


Figure 5. a–f) Potential maps of the micro-LED device at selected forward bias voltages.

make electron holography difficult to quantify, especially as it is dependent on the material, the dopant concentration and of course the energy and species of the ions used.^[42–44] In addition, the potentials measured in doped specimens can be higher when they are electrically contacted as this allows the electron beam induced charging to be removed.^[45] In general, the authors avoid quantifying the measured potentials and prefer to make relative measurements comparing results acquired from similar specimens.

The second effect of specimen preparation is that the specimen surfaces can be conducting which means that current can flow either side of the diode in the TEM specimen. Therefore, this needs to be limited to as much as possible. The parallel resistance on either side of the specimen will not change how the potential is applied across the diode, but if it isn't controlled then the sample will draw too much current and can be damaged from heating. The key is to avoid resistances in series, which would lead to only part of the total potential being applied across the region of interest.

There is no systematic study of the electron holography artefacts in AlGaInP in the literature. In these experiments, low energy ions were used for preparation, then the surfaces were cleaned at 2 kV. From these observations, the inactive thickness for the AlGaInP seems to be low due to the high dopant concentrations and perfect cubic structure of the specimen. The effect of the surfaces has also been limited by using a very thick specimen. Finally, the specimen preparation geometry has been carefully optimized to limit the conductivity of the surfaces and potential short circuit paths. The inset in Figure 6a shows the IV characteristics measured in situ. After preparation for TEM examination, a small amount of current flow is measured at reverse bias voltages which is from surface damage.^[45]

Figure 4b shows an image of the specimen in the electron microscope at low magnification. The bright line is the electron

hologram which arises from the overlapping of the electron wave each side of the biprism. Figure 4c shows a reference electron hologram with a fringe spacing of 1.6 nm and Figure 4d a magnified region showing the fringes. The electron counts and contrast of the hologram that was acquired for 8 seconds can be seen in Figure 4e. Here, 180 electrons (e^-) have been detected on a pixel of size 0.188 nm^2 which corresponds to a low beam current of $6.3 \text{ e}^- \text{ \AA}^{-2} \text{ s}^{-1}$. Figure 4f shows a detail of an electron hologram taken from the region of interest. It is clear that by looking at the 355 nm thick specimen using 200 kV electrons and a low beam current, not enough electrons are detected to clearly observe the fringes. This problem can be solved by acquiring a stack of electron holograms, which are then combined to provide phase images with higher sensitivity. In these experiments, stacks of 16 electron holograms, each acquired for 8 seconds were used to provide potential maps with a useful signal to noise ratio.^[46]

Stacks of electron holograms were acquired of the region of interest from 0 to 3.5 V applied forward bias in steps of 0.25 V, then a final hologram was acquired back at 0 V. The phase images were then used to calculate potential maps with a spatial resolution of 5 nm given by the size of the mask used during the reconstruction. As the inactive thickness is unknown for AlGaInP, the measured potential maps will not be accurate. However, the relative changes in potential can be compared, which is one of the advantages of performing in situ electrical biasing. **Figure 5a–f** shows potential maps of the region of interest for selected applied voltages. As expected, the QWs can be observed as the bright lines arising from the differences in MIP between GaInP and AlGaInP layers. The dark contrast at the bottom of the maps arises from active p-type dopants in the AlGaInP and the bright contrast at the top from the n-type doped AlGaInP region. To account for the slow changing fields that occur above and below the specimen as it is biased, the potential has been flattened in the p-type region. At 0 V bias a large step in potential can be observed across

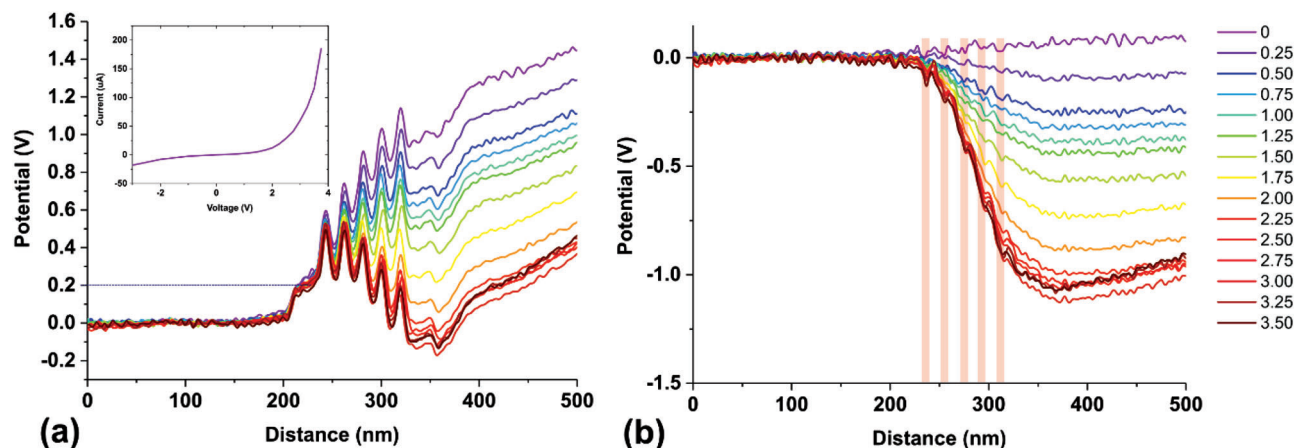


Figure 6. a) Potential profiles as a function of applied forward bias voltage. The IV characteristics of the thin TEM sample are shown in the inset. b) The potential profiles acquired at various voltages with the 0 V profile subtracted to show only the electrical changes in the specimen and remove the contributions of the mean inner potential and artefacts from specimen thickness changes and dynamical diffraction. The position of the QWs are indicated. The forward bias values are in V.

the QW structures and at increased forward bias voltage this step in potential is reduced.

2. Results and Discussion

The potential profiles averaged from the region indicated in Figure 5a are shown in Figure 6a. These reveal more clearly the reduction in potential across the QWs as the forward bias voltage is increased until a saturation is reached at 2.25 V. This is in agreement with the images of the diode emission shown in Figure 2a–c which suggest that the region of the diode examined in the experiment under the electrical contact reaches saturation between 2.0 and 3.0 V.

The gradient in the potential profiles for the top n-type region is due to the unintended presence of dynamical diffraction, which was difficult to observe in the specimen before data acquisition due to its thickness and the low electron beam current that was used. The inset in Figure 6a shows the IV characteristics of the diode after FIB preparation indicating that it still behaves as a diode. Although the electrical characteristics have been modified, for example the presence of a current at reverse bias which flows in parallel across the residual surface damage, we can observe that the diode begins to conduct current at 1.0 V in agreement with the ex situ measurements. In terms of the potential profiles, Figure 6a also shows that at 1.5 V which is just before the onset of emission in the ex situ measurements there is still a slight potential gradient across the QWs. A key point is that the potential across the QWs becomes flat at 1.75 V which is the voltage at which the micro-LED begins to emit light.

To remove the contributions of the MIP and artefacts from dynamical diffraction, it is possible to subtract each potential profile at forward bias from the initial 0 V profile that was acquired before biasing. Figure 6b shows the reduction in potential across the p–n junction as a function of applied forward bias voltage. Here it can be seen that change in the step in potential increases relatively quickly until 0.5 V, then more slowly up until a voltage of 1.5 V which corresponds to the voltage where emission occurs. After this, larger changes in potential are observed until satura-

tion at 2.25 V. An additional observation is that the forward bias changes the step in electrical potential across the QWs arising from the active dopants, however, no absolute change of potential is observed in the QWs themselves showing that the applied forward bias voltage only affects the free carriers associated with doping in the micro-LED device.

From the nominal alloy concentrations, the MIP calculated from the DFT simulations is expected to be 13.0 V for the $\text{Al}_{0.35}\text{G}_{0.15}\text{In}_{0.5}\text{P}$ p and n type layers, 13.2 V for the $\text{Al}_{0.25}\text{G}_{0.25}\text{In}_{0.5}\text{P}$ undoped layers either side of the QWs and 13.7 V in the $\text{G}_{0.39}\text{In}_{0.61}\text{P}$ QWs. Figure 6a shows a step in potential, indicated by the dashed line of 0.2 ± 0.05 V between the doped p-type region and the undoped region, suggesting directly from the MIP that the alloy composition of the diode is as expected. From the DFT calculations a potential difference of 0.5 V would be expected between the QWs and the QBs. However, a value of 0.25 ± 0.05 V is measured which can in part be explained by the EDX results that reveal the presence of Al in the QWs and by the spatial resolution of the technique compared to these regions of interest.

To help the interpretation of the measured potentials in the device, simulations were performed. Here the band structure is important as it takes into account various properties including the potential profile arising from the active dopants and the offsets from the different layers. Electron holography does not measure the band offsets, but the differences in MIP indicate clearly the position of the QWs in relation to the distribution of potential arising from the active dopants. Figure 7 shows the simulations of the conduction band compared to the negative of the potential profile, which we use for qualitative visualization of the experimental results where,

$$V = -\frac{1}{q}E \quad (2)$$

and q is the charge on an electron and E is the potential energy in eV. Figure 7a shows the negative potential profile and a gradient is observed across the QW structures at a forward bias voltage of 1.5 V just before light emission was observed in the

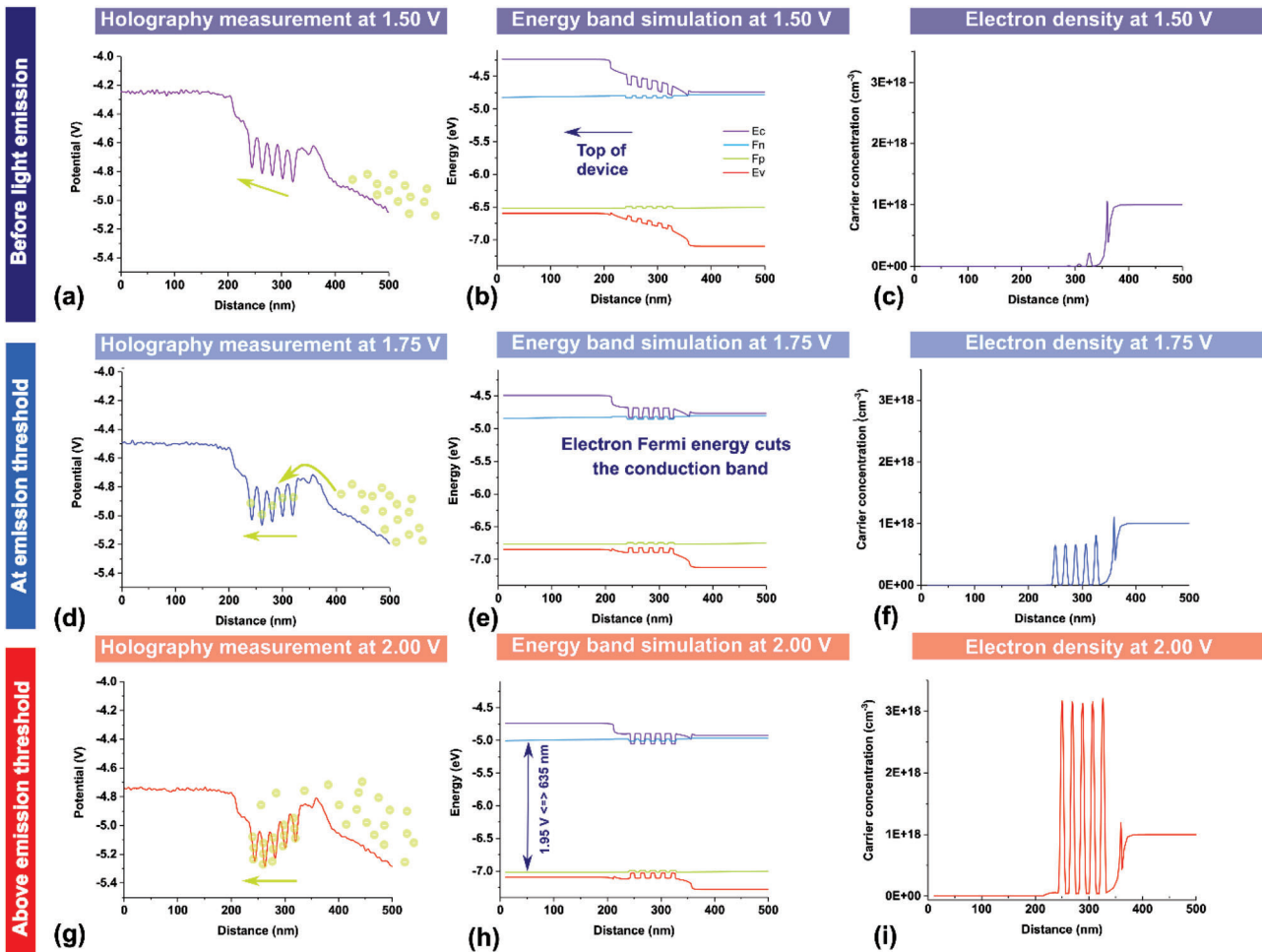


Figure 7. a) The negative of the measured potential profile measured at 1.5 V by electron holography. b) Simulations of the band energies at a forward bias voltage of 1.5 V just before light emission. c) Simulations of the electron density at 1.5 V. d) Negative of the potential profile measured at 1.75 V. e) Simulation of the band energies at a forward bias voltage of 1.75 V above the light emission detection by ex situ measurements. f) Simulation of the electron density at 1.75 V. g) Negative of the potential profile measured at 2.0 V. h) Simulation of the band energies at a forward bias voltage of 2.0 V which is above the theoretical emission voltage for a diode of 635 nm. i) Simulation of the electron density at 2.0 V.

ex situ measurements. Here, the offset of the measured potential at the top of the device has been fixed at the value given from the simulated conduction band. The simulated conduction band, E_c , the Valence band E_v and the electron and hole Fermi levels, F_n and F_p , respectively at a forward bias voltage of 1.5 V are shown in Figure 7b. As observed in the experimental results, a positive gradient going from the bottom toward the top of the device can be seen which would prevent the injected electrons from reaching the QWs. In order for the device to emit light, both electrons and holes are required to be present in the QWs to provide radiative recombination. Figure 7c shows a simulation of the electron density in the structure at a forward bias voltage of 1.5 V and few electrons are observed in the QWs, the maximum value being $2 \times 10^{17} \text{ cm}^{-3}$ in the first QW and then much fewer in the subsequent ones.

Figure 7d shows the electron holography results at a forward bias of 1.75 V which is just above the threshold voltage needed for light emission from the ex situ opto-electrical measurements. Here the QWs are aligned at the same value of potential. The sim-

ulations for a forward bias voltage of 1.75 V are in agreement and show that the QWs are aligned at the same energy and the electron Fermi level now cuts the conduction band. The simulation of the electron density shown in Figure 7f now reveals an average concentration of $6.2 \times 10^{17} \text{ cm}^{-3}$ electrons in all of the QWs. The simulations of the hole density that are not shown here show the same trend with a value of $5.5 \times 10^{17} \text{ cm}^{-3}$.

From the Planck equation, an applied voltage of 1.95 eV is required to obtain the expected 635 nm emission.^[47] Therefore at bias voltages of 1.50 and 1.75 V, additional thermal energy is also needed for the carriers to reach the QW. At 1.50 V the electrons and holes statistically have little chance of reaching the QWs, whereas at 1.75 V, even though the hole Fermi level doesn't yet cut the valence band, there are sufficient carriers due to thermal excitation in the QWs to provide detectable light emission.

The important observation in this multi-QW system is that at 1.75 V the bands are flattened which means that all of the wells will statistically have the same population of carriers within them as they are all equally close to the Fermi levels. We can observe

from Figure 7b, which shows the simulations of the energy bands at a forward bias voltage of 1.5 V, for the single QW at the top of the device, the valence band is close to the hole Fermi level, but the conduction band is far from the electron Fermi level. Whereas, for the QW at the bottom of the device the conduction band is closer to the electron Fermi level but the valence band is far from the hole Fermi level. In Figure 7e, which shows the bands at 1.75 V, the alignment, or flattening of the bands means that all of the QWs are close to the Fermi levels and thus radiative recombination can occur in all of the QWs simultaneously.

Finally, Figure 7g shows the electron holography results for a forward bias voltage of 2.0 V which is now above the theoretical threshold for emission. From the simulations shown in Figure 7h, we can see that the conduction band cuts the electron Fermi level, and the valence band is very close to the hole Fermi level. Now the emission of the diode is strong which can be seen in Figure 7i where simulations suggest that a carrier density of $3.1 \times 10^{18} \text{ cm}^{-3}$ electrons (and $3.0 \times 10^{18} \text{ cm}^{-3}$ holes) in the QWs is expected.

3. Conclusion

Thus, we have demonstrated that off-axis electron holography can be used to provide dynamic measurements of the electrostatic potential with nm-scale resolution of a fully processed micro-LED device that has been operated in situ in the TEM. The interplay between the doped regions relative to the quantum wells is key in order to understand the efficiency of the device relative to the injection current. By measuring the local potentials in the active area as a function of forward bias it has been possible to observe the alignment of the quantum wells in the device as it begins to emit light and confirm these observations by simulation. This alignment is key in multi QW systems in order for the Fermi level to cut the conduction and valence bands simultaneously in all the different wells at the lowest forward bias voltage possible.

The ability to observe the potentials in situ during device development will allow better understanding of malfunctioning devices or failure analysis, to investigate the effects of doping, or to look at differently performing regions in the same device, such as edge effects and performances close and far from electrical contacts. In this case, a simple red micro-LED with known good properties has been examined directly under the cathode region, and the results are remarkably coherent with both the electro-optical measurements and the simulations. Using these methods, it will now be possible to assess the distribution of potentials across the electrical junctions in different opto-electronic devices, to visualize the discrepancies between current onset and the luminance onset or the presence of charge trapping in defective regions. More complicated structures, such as quantum cascade lasers (QCL), vertical cavity surface emitting lasers (VCSELs) or even tunnel-junction LED structures could be also examined.

Off-axis electron holography measures the differences in MIP (volume-averaged potential) in the specimen in the different regions of the diode. It also contains information about the doping, the effects of strain and for polar materials, the piezoelectric potentials and the corresponding Stark effect. In this work we observe a qualitative match between the simulated conduction band and the negative of the potential profiles. However,

we intend to extend this work to understand if the experimental measurements of the potentials can be taken further to help interpret and calculate values of the band-offsets. The goal being to obtain a more accurate understanding of the complex interplay between dopants, piezoelectric fields and strain in different materials, their effect the conduction band and properties of the device.

From the point of view of the experimental work, improvements in the signal to noise ratio can still be expected from better, larger and more efficient detectors and by acquiring larger hologram stacks. In addition, a full assessment of different ion species^[42,44] for specimen preparation needs to be performed in order to optimize the applied biasing in the TEM. Ideally these experiments would be fully automated which would allow the acquisition of larger and more complete data sets and allow these experiments to be performed more routinely.

4. Experimental Section

Device Processing: AlInGaP/InGaP based hetero-structures were grown by metal organic chemical vapour deposition on 10° off-axis [100] GaAs substrates. The process starts with the transfer of red emitting epilayers onto receiving Si substrates. The Si substrates were metallized with Ti bonding layer deposited by physical vapour deposition and followed by chemical-mechanical polishing to enable planarization. Then the GaAs substrate and the sacrificial layers were removed by highly selective wet etching techniques. The remaining thickness of the hetero-structure was $\approx 900 \text{ nm}$ as shown in Figure 1. The device fabrication begins with the deposition of Ti/Pt as a p-type contact in a square-like geometry by e-beam evaporation. The definition of the mesa structure then ensues with successive deposition of a SiN/SiO₂ bilayer hard mask (HM) by plasma-enhanced chemical vapor deposition (PECVD). The bi-layer HM was subsequently etched by CHF₃ and SF₆-based induced coupled plasma (ICP). Thereafter, the III-V hetero-structure was etched down to the Ti bonding interface with a SiCl₄/Ar-based plasma. The remaining HM was removed by dry etching. Next, the devices were passivated by a PECVD-SiN layer, which was later selectively etched with SF₆-based ICP. This passivation allows for the Ti/Au-based deposition for both contacts in the PECVD chamber.

Opto-Electrical Characterization: IVL measurements were performed using a Keithley 2410 SMU. The luminance was measured with a 1 cm^2 Hamamatsu photodiode placed above the micro-LED. The micro-PL signal was measured with a 514 nm laser excitation through a 10x objective and a Horiba LabRAM HR spectrometer.

Transmission Electron Microscopy: HAADF STEM and EDX experiments were performed using a probe FEI Titan Themis operated at 200 kV. The EDX data was quantified using the Cliff-Lorimer method. Here the metal fraction (Al, Ga, In) was quantified as the Nitrogen edge at 420 eV was strongly affected by absorption. The off-axis electron holography experiments were performed using a FEI Titan Ultimate operated at 200 kV combined with the use of a low beam current to avoid damaging the specimen. The stacks of electron holograms were reconstructed using the Holoview software that was written at CEA LETI. To calculate the electrostatic potential from the phase, the specimen thickness was measured by convergent beam electron diffraction. More details about the specimen preparation and off-axis electron holography experiments were given in the main body of this manuscript as this was the focus of this work.

Simulations: These were performed using the commercially available Synopsys LaserMod software. The input was taken from the design of the micro-LED. The electron-hole band structures were calculated via a KP perturbation theory providing information about the density of states, as well as energy and strength of optical transitions. In our study, quantum wells were assumed to be square, uncoupled and identical. The simulations were for bulk material and do not take into account the surfaces of the thin TEM specimen.

Acknowledgements

This work, performed on the Platform for NanoCharacterisation (PFNC) of CEA, was supported by the "Recherche Technologique de Base" Program of the French Ministry of Research.

Conflict of Interest

The authors declare no conflict of interest.

Data Availability Statement

The data that support the findings of this study are available from the corresponding author upon reasonable request.

Keywords

electron holography, electrostatic potentials, in situ transmission electron microscopy, LED, optoelectronics

Received: April 26, 2023

Published online:

- [1] H.-W. Chen, J.-H. Lee, B.-Y. Lin, S. Chen, S.-T. Wu, *Light Sci. Appl.* **2018**, 7, 17168.
- [2] Y. Huang, G. Tan, F. Gou, M.-C. Li, S.-L. Lee, S.-T. Wu, *J. Soc. Inf. Disp.* **2019**, 27, 387.
- [3] C. D'Souza, H.-G. Yuk, G. H. Khoo, W. Zhou, *Compr. Rev. Food Sci. Food Saf.* **2015**, 14, 719.
- [4] F. Palma, G. Baldelli, G. F. Schiavano, G. Amagliani, M. P. Aliano, G. Brandi, *Atmosphere* **2022**, 13, 1411.
- [5] P. Tian, J. J. D. McKendry, Z. Gong, B. Guilhabert, I. M. Watson, E. Gu, Z. Chen, G. Zhang, M. D. Dawson, *Appl. Phys. Lett.* **2012**, 101, 231110.
- [6] F. Olivier, S. Tirano, L. Dupré, B. Aventurier, C. Largeron, F. Templier, *J. Lumin.* **2017**, 191, 112.
- [7] R. Alcotte, M. Martin, J. Moeyaert, R. Cipro, S. David, F. Bassani, F. Ducroquet, Y. Bogumilowicz, E. Sanchez, Z. Ye, X. Y. Bao, J. B. Pin, T. Baron, *APL Mater.* **2016**, 4, 046101.
- [8] Z. Liu, M. Martin, T. Baron, S. Chen, A. Seeds, R. Penty, I. White, H. Liu, C. Hantschmann, M. Tang, Y. Lu, J.-S. Park, M. Liao, S. Pan, A. Sanchez, R. Beanland, *J. Light. Technol.* **2020**, 38, 240.
- [9] S. D. Lester, F. A. Ponce, M. G. Craford, D. A. Steigerwald, *Appl. Phys. Lett.* **1995**, 66, 1249.
- [10] D. Cherns, W. T. Young, M. Sanders, J. W. Steeds, F. A. Ponce, S. Nakamura, *Philos. Mag. A* **1998**, 77, 273.
- [11] F. A. Ponce, D. Cherns, W. T. Young, J. W. Steeds, *Appl. Phys. Lett.* **1996**, 69, 770.
- [12] J. L. Rouviere, M. Arlery, B. Daudin, G. Feuillet, O. Briot, *Mater. Sci. Eng. B* **1997**, 50, 61.
- [13] D. Cherns, J. Barnard, F. A. Ponce, *Solid State Commun.* **1999**, 111, 281.
- [14] J. S. Barnard, D. Cherns, *J. Electron Microsc.* **2000**, 49, 281.
- [15] M. Takeguchi, M. R. McCartney, D. J. Smith, *Appl. Phys. Lett.* **2004**, 84, 2103.
- [16] Z. H. Wu, M. Stevens, F. A. Ponce, W. Lee, J. H. Ryou, D. Yoo, R. D. Dupuis, *Appl. Phys. Lett.* **2007**, 90, 032101.
- [17] L. Zhou, D. A. Cullen, D. J. Smith, M. R. McCartney, A. Mouti, M. Gonschorek, E. Feltn, J. F. Carlin, N. Grandjean, *Appl. Phys. Lett.* **2009**, 94, 121909.
- [18] F. A. Ponce, *Ann. Phys.* **2011**, 523, 75.
- [19] B. Samuel, D. Cooper, N. Rochat, A. Mavel, F. Barbier, A. Dussaigne, *J. Appl. Phys.* **2021**, 129, 173105.
- [20] D. Cooper, V. Boureau, A. Even, F. Barbier, A. Dussaigne, *Nanotechnology* **2020**, 31, 475705.
- [21] V. Boureau, D. Cooper, *J. Appl. Phys.* **2020**, 128, 155704.
- [22] D. Cooper, V. Fan Arcara, B. Damilano, L. Amichi, A. Mavel, N. Rochat, G. Feuillet, A. Courville, S. Vézian, J. Duboz, *J. Appl. Phys.* **2021**, 130, 025704.
- [23] Y. Boussadi, N. Rochat, J.-P. Barnes, B. B. Bakir, P. Ferrandis, B. Masenelli, C. Licitra, *J. Lumin.* **2021**, 234, 117937.
- [24] X. Guo, E. F. Schubert, *J. Appl. Phys.* **2001**, 90, 4191.
- [25] L. Amichi, I. Mouton, V. Boureau, E. Di Russo, P. Vennegues, P. De Mierry, A. Grenier, P.-H. Jouneau, C. Bougerol, D. Cooper, *Nanotechnology* **2019**, 31, 045702.
- [26] A. Tonomura, *Rev. Mod. Phys.* **1987**, 59, 639.
- [27] M. R. McCartney, D. J. Smith, *Annu. Rev. Mater. Res.* **2007**, 37, 729.
- [28] J. C. H. Spence, *Acta Crystallogr. A* **1993**, 49, 231.
- [29] M. O'Keefe, J. C. H. Spence, *Acta Crystallogr. A* **1994**, 50, 33.
- [30] M. Y. Kim, J. M. Zuo, J. C. H. Spence, *Phys. Status Solidi A* **1998**, 166, 445.
- [31] R. S. Pennington, C. B. Boothroyd, R. E. Dunin-Borkowski, *Ultramicroscopy* **2015**, 159, 34.
- [32] P. Kruse, A. Rosenauer, D. Gerthsen, *Ultramicroscopy* **2003**, 96, 11.
- [33] P. Kruse, M. Schowalter, D. Lamoen, A. Rosenauer, D. Gerthsen, *Ultramicroscopy* **2006**, 106, 105.
- [34] A. C. Twitchett, R. E. Dunin-Borkowski, P. A. Midgley, *Phys. Rev. Lett.* **2002**, 88, 238302.
- [35] D. Cooper, C. Ailliot, J.-P. Barnes, J.-M. Hartmann, P. Salles, G. Benassayag, R. E. Dunin-Borkowski, *Ultramicroscopy* **2010**, 110, 383.
- [36] D. Cooper, C. Ailliot, R. Truche, J.-P. Barnes, J.-M. Hartmann, F. Bertin, *J. Appl. Phys.* **2008**, 104, 064513.
- [37] W. D. Rau, P. Schwander, F. H. Baumann, W. Höppner, A. Ourmazd, *Phys. Rev. Lett.* **1999**, 82, 2614.
- [38] M. A. Gribelyuk, M. R. McCartney, J. Li, C. S. Murthy, P. Ronsheim, B. Doris, J. S. McMurray, S. Hegde, D. J. Smith, *Phys. Rev. Lett.* **2002**, 89, 025502.
- [39] M. R. McCartney, M. A. Gribelyuk, J. Li, P. Ronsheim, J. S. McMurray, D. J. Smith, *Appl. Phys. Lett.* **2002**, 80, 3213.
- [40] D. Cooper, A. C. Twitchett, P. K. Somodi, P. A. Midgley, R. E. Dunin-Borkowski, I. Farrer, D. A. Ritchie, *Appl. Phys. Lett.* **2006**, 88, 063510.
- [41] P. K. Somodi, A. C. Twitchett-Harrison, P. A. Midgley, B. E. Kardynał, C. H. W. Barnes, R. E. Dunin-Borkowski, *Ultramicroscopy* **2013**, 134, 160.
- [42] D. Cooper, J.-M. Hartmann, N. Gambacorti, *J. Appl. Phys.* **2011**, 110, 044511.
- [43] D. Cooper, R. Truche, J.-L. Rouviere, *Ultramicroscopy* **2008**, 108, 488.
- [44] D. Cooper, F. Bertin, P. Salles, G. Benassayag, *Appl. Phys. Lett.* **2008**, 93, 043510.
- [45] D. Cooper, R. Truche, A. Twitchett-Harrison, R. Dunin-Borkowski, P. Midgley, *J. Microsc.* **2009**, 233, 102.
- [46] V. Boureau, R. McLeod, B. Mayall, D. Cooper, *Ultramicroscopy* **2018**, 193, 52.
- [47] D. K. Hillman, G. E. Smith, *IEEE Spectr* **1968**, 5, 62.